

## Vibrational and defect states in SnO<sub>x</sub> nanoparticles

Cedrik Meier,<sup>a)</sup> Stephan Lüttjohann, Vasyl G. Kravets, Hermann Nienhaus, and Axel Lorke  
*Experimental Physics, University of Duisburg–Essen, Lotharstrasse 1, D-47048 Duisburg, Germany*

Pascal Ifeacho, Hartmut Wiggers, and Christof Schulz  
*Combustion and Gas Dynamics, University of Duisburg–Essen, Lotharstrasse 1, D-47048 Duisburg, Germany*

Marcus K. Kennedy and F. Einar Kruis  
*Departement of Engineering Sciences, University of Duisburg–Essen, Bismarckstrasse 81, D-47057 Duisburg, Germany*

(Received 4 November 2005; accepted 12 April 2006; published online 15 June 2006)

We have studied SnO<sub>x</sub> nanoparticles fabricated by gas-phase condensation and in-flight sintering using Raman and photoluminescence (PL) spectroscopy. We are able to identify various vibrational states of the rutile phase of the SnO<sub>x</sub> crystal. By thorough analysis of the vibrational modes, we are able to determine the bond lengths of the O–O and Sn–O bonds for the substoichiometric SnO<sub>1.5</sub>, leading, together with x-ray diffraction data, to a full characterization of the SnO<sub>1.5</sub> lattice. In absorption and photoluminescence spectra, we observe a finite density of states inside the band gap due to oxygen vacancies, giving rise to a midgap luminescence peak. Our results suggest that the defect related luminescence efficiency is limited by nonradiative recombination processes and by the oxygen vacancy density. We therefore conclude that the PL intensity has a maximum around a stoichiometry of SnO<sub>1.7</sub>. © 2006 American Institute of Physics. [DOI: 10.1063/1.2203408]

### I. INTRODUCTION

Oxidic semiconductors, namely, ZnO and SnO<sub>x</sub>, have recently gained a large amount of interest as efficient optical materials.<sup>1,2</sup> Due to their large band gaps<sup>3,4</sup> and exciton binding energies,<sup>2,5</sup> they are attractive as light emitters for the ultraviolet-visible (UV-VIS) spectral range. Nanostructures formed from these materials, such as nanoparticles or nanorods, are especially interesting and have potential use as phosphors for solid-state lighting.<sup>6</sup> For such applications, the oxygen vacancy related defect band can be used for down-conversion of UV or blue light from a light emitting diode into the green (ZnO) (Refs. 7 and 8) or red (SnO<sub>x</sub>) region of the spectrum. These spectral bands are interesting for tri- and tetrachromatic phosphors which achieve better color rendering indices (CRIs) than conventional phosphors.<sup>6</sup> In comparison to organic phosphors, oxidic semiconductors exhibit also a much better long-term stability.

While ZnO nanostructures have attracted a lot of attention recently, the potential of SnO<sub>x</sub> nanoparticles has not been fully exploited yet. It is the aim of this paper to present a detailed study of the chemical, optical and vibrational properties of SnO<sub>x</sub> nanoparticles with oxygen compositions of  $1.5 \leq x \leq 1.7$ . We investigate these properties as a function of the size and the oxygen stoichiometry.

### II. EXPERIMENTAL DETAILS

The particles are formed by gas-phase condensation using N<sub>2</sub> as a carrier gas and SnO as an evaporation source. The SnO is sublimated in a tube furnace operated at 800 °C and forms SnO nanoparticles upon cooling down when leav-

ing the furnace. A differential mobility analyzer (DMA) is used for particle size separation. Before the particles are deposited on a substrate, they are being exposed to another furnace for in-flight sintering. Here, an oxygen flow can be added, so that nanoparticles with different oxygen compositions can be formed depending on the furnace temperature and oxygen flow. We have realized nanoparticles with sizes between 5 and 20 nm and oxygen stoichiometries of  $x=1.5$  and  $x=1.7$ . Details about the fabrication process can be found elsewhere.<sup>9,10</sup> Furthermore, SnO<sub>x</sub> particles were synthesized in a low pressure H<sub>2</sub>/O<sub>2</sub>/Ar premixed flame reactor with a process that has been previously described elsewhere.<sup>11</sup> The oxygen concentration during synthesis could be tuned to yield stoichiometries of  $1.4 \leq x \leq 2$ , whereby a stoichiometry of  $x=1.7$  was used for this investigation.

For the Auger electron spectroscopy (AES), the particles were deposited on thin films (250–300 Å) of Pd on Si (111). For transmission electron microscopy (TEM) measurements, the particles were sampled on a carbon TEM grid. For all other experiments, the particles were deposited on thick Au films on Si (111).

For the AES measurements, the primary electrons had an energy of 3 keV. The spectra were recorded in the first derivative mode using a cylindrical analyzer and a channeltron. X-ray diffraction measurements were obtained from a synchrotron radiation source at a wavelength of  $\lambda=1.55$  Å. For the Raman spectroscopy, we used the 5145 Å line of an Ar<sup>+</sup>-ion laser. The optical pumping power on the sample was ~40 mW and the spot diameter was ~100 μm. The light was collected in backscattering geometry and dispersed in a triple spectrometer ( $f=600$  mm) operated in subtractive mode. A charge coupled device (CCD) was used to collect

<sup>a)</sup>Electronic mail: cedrik.meier@uni-due.de

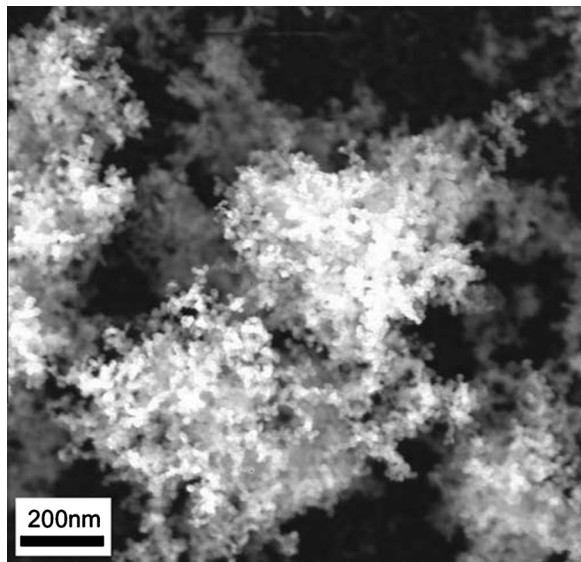


FIG. 1. Scanning electron microscopy (SEM) image of  $\text{SnO}_{1.5}$  nanoparticles.

the data. The spectral resolution achieved with this setup was  $\sim 1 \text{ cm}^{-1}$ . The optical absorption spectroscopy was performed by measuring the reflectivity of the samples using an Al substrate as a reference. The absorbance was obtained by applying the Kubelka-Munk algorithm. For photoluminescence (PL), a continuous wave (cw) frequency-doubled Ti:Sa laser operated at  $\lambda=400 \text{ nm}$  was used as an excitation source. The light was dispersed in a Czerny-Turner single grating monochromator and detected using a liquid nitrogen cooled CCD.

### III. RESULTS AND DISCUSSION

#### A. Structural and chemical characterizations

A scanning electron microscopy (SEM) image is shown in Fig. 1. It can be seen that the particles form loosely agglomerated structures of fractal shape, consisting of nearly spherical primary particles. Also, the image demonstrates well that the particles have a narrow size distribution due to the size selection in the DMA.

A typical TEM micrograph is shown in Fig. 2. Again, the monodispersity is well visible. Also, it can be seen that the primary particles are only loosely connected and do not form a large extended crystalline structure. The grain boundaries between the individual particles are well visible. This confirms that these particles are indeed independent structures, and that for their electronic or vibronic properties the primary particle size is the relevant length scale.

Auger electron spectra have been recorded from the nanoparticle samples as well as from bulk, i.e., non-nanoscale  $\text{SnO}_2$  pellets. This way, the chemical composition and sample surface contamination could be monitored.

The AES results are shown in Fig. 3. Several features can be identified. At  $\sim 421$  and  $\sim 429 \text{ eV}$  the Sn (*MNN*) doublet is found in all samples. The O (*KLL*) transition is observed at  $510 \text{ eV}$ . In addition to these structures we find for the nanoparticle samples a small peak at  $\sim 272 \text{ eV}$  due to the C (*KLL*) Auger transition. For the bulk  $\text{SnO}_2$  sample, this

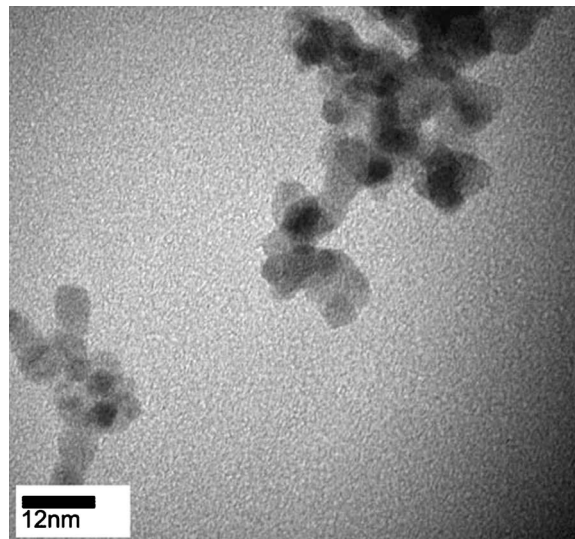


FIG. 2. Transmission electron microscopy (TEM) image of  $\text{SnO}_{1.5}$  nanoparticles sampled on a TEM grid.

structure is much more pronounced. This structure is due to residual contamination by hydrocarbon during sample transfer and synthesis. The fact that this peak is much less pronounced than the Sn peak in the nanoparticle samples demonstrates the purity of the synthesized nanocrystalline samples. The structure seen at  $333 \text{ eV}$  arises from the Pd (*MNN*) transition and is due to the Pd:Si substrate used.

The ratio between the oxygen peak and the low energy Sn peak can be used to determine the oxygen stoichiometry of the sample. As a reference, we have used the value measured for the bulk sample as  $\text{SnO}_2$ . For the as-synthesized samples we find a chemical composition of  $\text{SnO}_{1.5}$ . The annealed samples show an increased oxygen content of  $\text{SnO}_{1.7}$ .

Because for the proper analysis of the Raman data it is essential to know the lattice structure, we have performed x-ray diffraction (XRD) on a  $\text{SnO}_{1.5}$  sample with  $d=20 \text{ nm}$  (see Fig. 4) and identified the observed features using Bragg's condition. Obviously, the tetragonal phase is dominant, with lattice constants  $a=4.746 \text{ \AA}$  and  $c=3.189 \text{ \AA}$ . The values for bulk  $\text{SnO}_2$  are  $a=4.737 \text{ \AA}$  and  $c=3.186 \text{ \AA}$ .<sup>12</sup> This

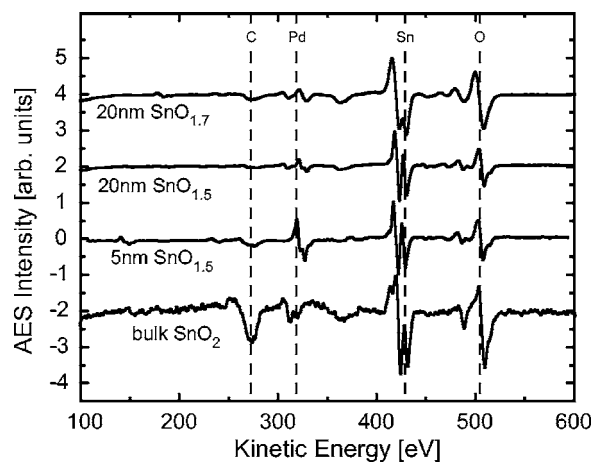


FIG. 3. Auger electron spectroscopy (AES) measurement of  $\text{SnO}_x$  particles sampled on a Pd surface.

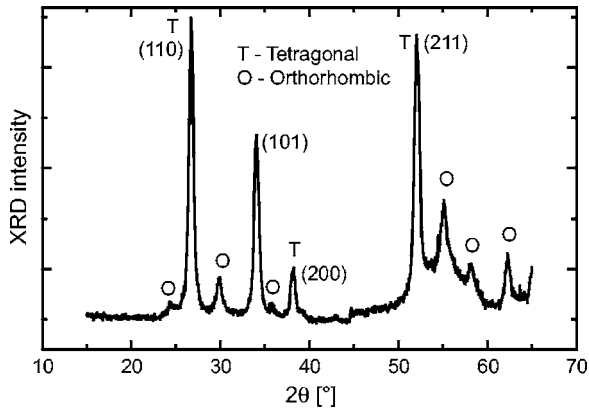


FIG. 4. X-ray diffraction measurement of  $\text{SnO}_{1.5}$  nanoparticles with  $d = 20$  nm.

means that despite the low oxygen composition in our samples the crystalline structure is still rutile and the volume of the conventional unit cell is only slightly increased by  $\sim 0.4\%$ . Apart from the tetragonal phase we also find a low concentration of orthorhombic crystals.

These results agree very well with the XRD measurements performed by Zhang and Gao<sup>13</sup> on  $\text{SnO}_2$  nanocrystals prepared by a sol-gel method. They also obtain a dominant rutile phase and an increase in the unit cell volume even for their much higher oxidation state. This reassures us that the  $\text{SnO}_2$  phonon dispersion relation will be a reasonable starting point for the analysis of the Raman spectra.

## B. Raman spectroscopy

Raman spectra of bulk crystalline  $\text{SnO}_2$  in rutile structure have been carried out in detail by Katiyar *et al.*<sup>14</sup> The Raman active modes for rutile  $\text{SnO}_2$  are the  $E_g$  ( $476\text{ cm}^{-1}$ ), the  $A_{1g}$  ( $638\text{ cm}^{-1}$ ), the  $B_{2g}$  ( $782\text{ cm}^{-1}$ ), and the  $B_{1g}$  ( $123\text{ cm}^{-1}$ ) mode. Although the  $B_{1g}$  mode is Raman active, its scattering intensity is at least three orders of magnitude lower than that of the  $A_{1g}$  mode and therefore it is not observed in most cases.<sup>14</sup>

More recently, nanoscopic  $\text{SnO}_2$  samples have been studied using Raman spectroscopy as well.<sup>15–17</sup> Zuo *et al.* find in addition to the bulk  $\text{SnO}_2$  Raman features two features at  $358$  and  $572\text{ cm}^{-1}$ . They assign those peaks to surface phonon modes.<sup>16</sup> The results obtained by Yu *et al.* are very similar. They observe three peaks not found for bulk  $\text{SnO}_2$  with Raman shifts of  $358$ ,  $574$ , and  $440\text{ cm}^{-1}$ .<sup>15</sup> While they also assign the first two peaks to interface/surface modes, they suggest that the spectral feature at  $440\text{ cm}^{-1}$  could be related to the presence of oxygen vacancies that make the otherwise Raman forbidden  $A_{2g}$  mode allowed due to reduced symmetry. Scott<sup>18</sup> has applied Matossi's<sup>19</sup> force constant model on  $\text{SnO}_2$  and derived for the frequency of the  $A_{2g}$  mode a value of  $455\text{ cm}^{-1}$ . This agrees well within the limits of the model with the result by Yu *et al.*<sup>15</sup> and supports the assumption that oxygen vacancies are responsible for the emerging of that line. The recent work by Chen *et al.* on nanocrystalline  $\text{SnO}_2$  does not show any evidence of the aforementioned peaks. Instead, the authors find a peak not

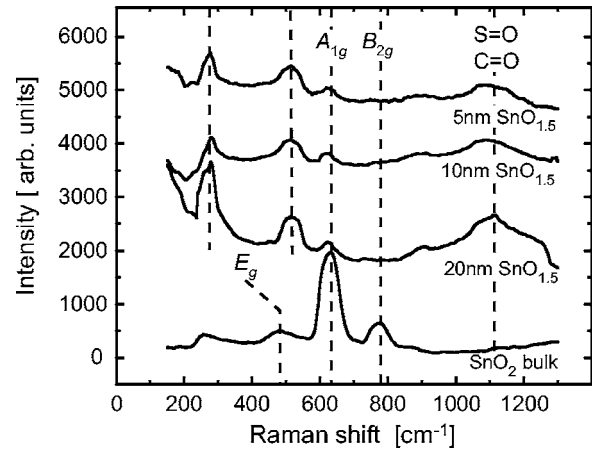


FIG. 5. Raman spectroscopy measurement of  $\text{SnO}_{1.5}$  nanoparticles with different particle diameters.

observed before at  $516.1\text{ cm}^{-1}$ . This peak is only found in the as-prepared samples and disappears after annealing.

While the work discussed above was focused on  $\text{SnO}_2$ , the scope of our study is the substoichiometric  $\text{SnO}_{1.5}$ . Our measurements for Raman spectra as a function of their size are shown in Fig. 5. We have measured particles with diameters of  $20$ ,  $10$ , and  $5\text{ nm}$  and a bulk  $\text{SnO}_2$  sample for reference. As the oxygen content ( $\text{SnO}_{1.5}$ ) of the particles was considerably lower than in the previous studies, we expect a much higher density of oxygen vacancies in our samples. We can easily identify the  $A_{1g}$ , the  $E_g$ , and the  $B_{2g}$  modes. While the  $E_g$  mode is only found in the bulk  $\text{SnO}_2$  sample, the  $B_{2g}$  mode can be seen with a very weak intensity around  $747\text{ cm}^{-1}$  for the  $10\text{ nm}$  and the  $5\text{ nm}$  samples. Moreover, for the nanocrystalline samples we observe two other bands not present in the bulk samples at  $275\text{ cm}^{-1}$  (referred to as band A in the following) and at  $515\text{ cm}^{-1}$  (band B).

While the  $A_{1g}$  and  $B_{2g}$  modes can be easily assigned, there are two possible interpretations for bands A and B. Band A ( $275\text{ cm}^{-1}$ ) might be identified as the  $B_{1g}$  mode and band B ( $515\text{ cm}^{-1}$ ) as the  $A_{2g}$  mode. Although both modes are Raman inactive in the bulk, one might argue that the reduction of the symmetry of the lattice due to the low oxygen stoichiometry makes these transitions possible. However, following Matossi's<sup>19</sup> model it is not possible to assign both modes to rutile lattice vibrational states. Therefore, either band A or band B is most likely a surface phonon state, similar to those found by Yu *et al.*<sup>15</sup> and Zuo *et al.*<sup>16</sup> for  $\text{SnO}_2$ .

Matossi's force constant model for the rutile structure delivers equations for each individual vibrational state. For convenience, we use his labeling of the vibrational frequencies, i.e.,  $\omega_1(A_{1g})$ ,  $\omega_2(A_{2g})$ ,  $\omega_3(B_{1g})$ , and  $\omega_4(B_{2g})$ . We will use the substitutions

$$x := \frac{k''}{m}, \quad (1)$$

$$y := \cos \psi \sin \psi, \quad (2)$$

where  $k''$  is the force constant for the O–O binding and  $m$  the mass of an oxygen atom.

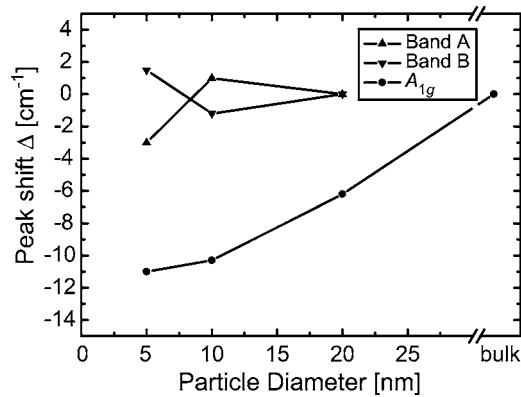


FIG. 6. Raman peak positions for bands A and B, and the  $A_{1g}$  peak as a function of particle diameter.

From the already assigned (see above) vibration modes  $A_{1g}$  and  $B_{2g}$ , we obtain the following equation:

$$\omega_4^2 - \omega_1^2 = 16xy. \quad (3)$$

Now, we need to assign the bands A and B.

If band A is assigned to the  $B_{1g}$  mode, one obtains from Matossi's model:

$$\omega_3^2 = 4x(1 - 2y). \quad (4)$$

Together with Eq. (3), this system of equations yields a bond angle  $\psi = 21.16^\circ$ . However, alternatively we can assign band B to the  $A_{2g}$  mode. This leads to the following equation:

$$\omega_2^2 = 4x(1 + 2y). \quad (5)$$

In turn, together with Eq. (3), one obtains a bond angle  $\psi = 12.59^\circ$ , different from the bond angle calculated from the assumption that band A is the  $B_{1g}$  mode. This means that one of the two assignments for bands A and B is incorrect. In the following, we will compare the obtained values for the bond angle to find the correct assignment.

The angle  $\psi$  in Eq. (2) is defined after<sup>19</sup> as the projection of the angle between an O–Sn and an O–O bond in the (100) plane of the lattice. For bulk  $\text{SnO}_2$ , we can determine  $\psi$  from the geometry of the lattice positions of the Sn and O atoms. The Sn atoms are located at (0,0,0) and  $(\frac{1}{2}, \frac{1}{2}, \frac{1}{2})$ . The O atoms are located at  $\pm(u, u, 0)$  and  $(\frac{1}{2} + u, \frac{1}{2} - u, \frac{1}{2})$ , with  $u = 0.307$ .<sup>12</sup> Therefore, one obtains

$$\psi = 45^\circ - \arctan \frac{2u - (1/2)}{1/2} = 32.15^\circ. \quad (6)$$

As we know from XRD that the lattice constants have only been slightly distorted, it seems reasonable to assume that the interpretation leading to a bond angle  $\psi$  closer to the bulk  $\text{SnO}_2$  is the correct one. We therefore suggest that band A observed at  $275 \text{ cm}^{-2}$  is the  $B_{1g}$  mode of the rutile lattice and band B at  $515 \text{ cm}^{-2}$  is a surface phonon mode. From this solution, we can determine the individual atom positions by solving Eq. (6) for  $u$  and find  $u = 0.347$ . Therefore, the Sn–O distance in the (110) plane is increased by 12%.

Therefore, from both XRD and Raman we are able to determine the entire lattice structure.

In the next paragraph, we want to discuss the influence of particle diameter on the Raman spectra. In Fig. 6 we have

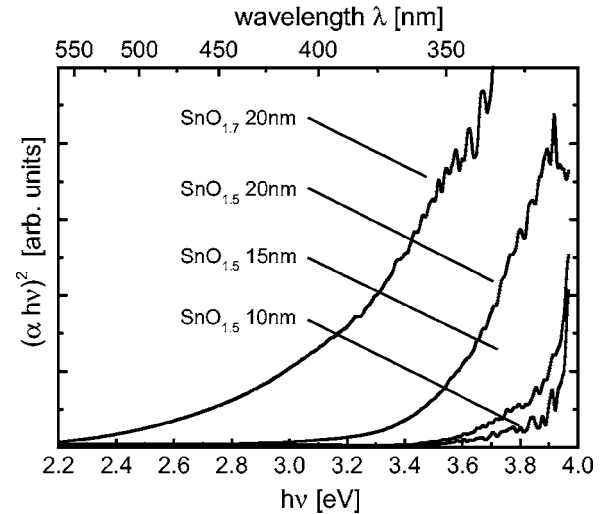


FIG. 7. Optical absorption of the  $\text{SnO}_x$  nanoparticles as a function of their size.

plotted the relative peak shifts of the  $A_{1g}$  mode, and bands A ( $B_{1g}$ ) and band B (surface phonon) as a function of particle size. It can be seen that only the  $A_{1g}$  mode shows a pronounced and systematic size effect. The other lines do not shift within the experimental resolution. These results can be analyzed in the framework of the phonon confinement picture as used for nanocrystalline silicon.<sup>20,21</sup> This model explains the shifts in phonon spectra by the dispersion of the phonon dispersion relation and a phonon wave vector mixing due to the reduced particle dimensions. In general, the shift in the Raman spectra reflects the slope of the dispersion relation in the high symmetry directions off the  $\Gamma$  point. However, for our substoichiometric  $\text{SnO}_{1.5}$ , the bulk phonon dispersion is not available. Only for bulk  $\text{SnO}_2$  calculated phonon dispersion curves have been calculated,<sup>14</sup> but even in this case some of the frequencies, e.g., for the  $B_{1g}$  mode, differ significantly from the frequencies determined experimentally in our work or those one obtains from Matossi's model.<sup>19</sup> However, for the  $A_{1g}$  mode Katiyar *et al.* find in the [001] direction a phonon branch with a strong negative slope. In the [011] direction the dispersion is nearly completely flat. This agrees well with our finding of a redshift of the  $A_{1g}$  line. For the  $B_{1g}$  mode they determine positive slopes in the [001] and the [011] directions and a frequency of  $100 \text{ cm}^{-1}$  at the  $\Gamma$  point. Our results lead to different conclusions. As we do not observe a significant peak broadening for the  $B_{1g}$  mode with decreasing particle size we suggest that the dispersion relation for this mode in  $\text{SnO}_{1.5}$  must be quite flat. However, this could only be confirmed by theoretical calculations that are beyond the scope of this paper.

### C. Optical absorption and photoluminescence

We have determined the optical absorption from diffusive reflection spectra using the Kubelka-Munk formula. The results for nanoparticle diameter between 10 and 20 nm and oxidation states of  $\text{SnO}_{1.7}$  and  $\text{SnO}_{1.5}$  are shown in Fig. 7. From a fit of the absorption data to

TABLE I. Band gaps for SnO<sub>x</sub> nanoparticles determined by absorption measurements.

Sample	$E_g$ (eV)
20 nm SnO <sub>1.7</sub>	3.10
20 nm SnO <sub>1.5</sub>	3.53
15 nm SnO <sub>1.5</sub>	3.80
10 nm SnO <sub>1.5</sub>	3.86

$$\alpha(\hbar\omega) \propto (\hbar\omega - E_g)^{1/2}, \quad (7)$$

we determine the band gap energies shown in Table I. For the SnO<sub>1.5</sub> particles, in Fig. 8 the band gap energies are plotted versus the particle diameter. It can be seen that with decreasing particle diameter the band gap increases. However, in the spectra the onset of interband absorption is quite soft in comparison to bulk semiconductors with a direct band gap. This is also evident from Fig. 8, where the change in band gap energy between the 20 and the 15 nm seems to be larger than what one would expect from an electronic confinement effect. This is caused by Urbach tail states due to a nonzero electronic density of states close to the band edges. For the 20 nm sample, this effect is quite strong and therefore it appears likely that the determined value for this sample might be too small. For the annealed sample with an increased oxygen content of SnO<sub>1.7</sub>, the band gap value determined from the fit of 3.1 eV is significantly smaller than the bulk value of SnO<sub>2</sub>. We therefore conclude that the annealing indeed leads to an increase of the Urbach tail states.

In the last paragraph, we want to present the results of the photoluminescence spectroscopy. We have excited the nanoparticles at a wavelength of  $\lambda=400$  nm, which is a typical wavelength of GaN-based light emitting diodes (LEDs) on which a phosphor coating could be applied for white light rendering. Our results are plotted in Fig. 9. We find a broad ( $\Delta E \approx 400$  meV) peak at an energy of  $E=2$  eV ( $\lambda=625$  nm). We find the center wavelength of the emission to be independent of the particle size, which suggests that the luminescence is caused by a defect band, most likely by the oxygen vacancies present in the samples. The fact that the 20 nm SnO<sub>1.5</sub> sample shows more intense photoluminescence under identical excitation conditions correlates with

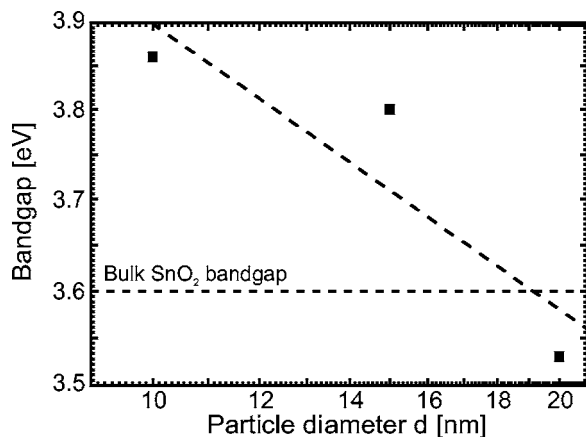
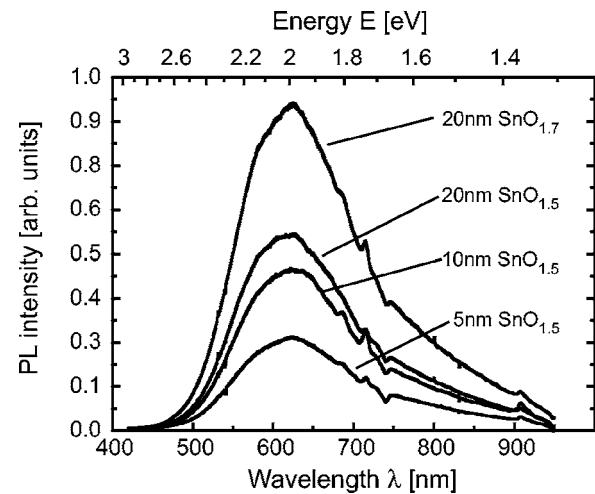
FIG. 8. Band gap of SnO<sub>1.5</sub> nanoparticles as a function of their size.

FIG. 9. Results of photoluminescence measurements for different particle sizes and oxidation states.

the observation of a high electronic density of states inside the band gap from the absorption measurements presented above.

For the 20 nm SnO<sub>1.7</sub> sample, we observe the highest photoluminescence intensity,  $\sim 72\%$  higher than for the SnO<sub>1.5</sub> sample. We attribute this increase in intensity to a lower rate of nonradiative recombinations in the SnO<sub>1.7</sub> sample due to a lower overall defect density. Our results suggest that the oxygen vacancy related photoluminescence should have a maximum intensity between oxygen stoichiometries of SnO<sub>1.5</sub> and SnO<sub>2</sub>. Obviously, in an ideal (i.e., thermodynamically limited) SnO<sub>2</sub> crystal, there is no defect related photoluminescence. If the number of oxygen vacancies is increased, the PL intensity will increase until nonradiative recombination processes will dominate.

#### IV. CONCLUSIONS

In summary, we have performed a comprehensive study of substoichiometric SnO<sub>x</sub> ( $1.5 \leq x \leq 1.7$ ) nanoparticles using optical spectroscopy. In Raman spectroscopy, we were able to observe the  $A_{1g}$ , the  $B_{1g}$ , and the  $B_{2g}$  modes as well as a surface phonon state. By applying a harmonic force constant model, we are able to determine the individual atom positions inside the conventional tetragonal SnO<sub>1.5</sub> unit cell. We find that the bond length of the Sn–O bonds is increased while the O–O bond length is decreased. Using absorption and photoluminescence spectroscopy we were able to show that the oxygen vacancies lead to a finite density of states inside the band gap, giving rise to nonradiative recombinations. We conclude that there is a stoichiometry around SnO<sub>1.7</sub> that leads to maximum photoluminescence efficiency of the oxygen vacancy band.

#### ACKNOWLEDGMENT

The authors gratefully acknowledge funding by the Deutsche Forschungsgemeinschaft (DFG) under Grant No. SFB 445—“Nanoparticles from the gas phase.”

- <sup>1</sup>Y. Wang, J. Ma, F. Ji, X. Yu, and H. Ma, *J. Lumin.* **114**, 71 (2005).
- <sup>2</sup>B. Yu, C. Zhu, and F. Gan, *Opt. Mater. (Amsterdam, Neth.)* **7**, 15 (1997).
- <sup>3</sup>M. Nagasawa and S. Shionoya, *Phys. Lett.* **22**, 409 (1966).
- <sup>4</sup>F. J. Arlinghaus, *J. Phys. Chem. Solids* **35**, 931 (1974).
- <sup>5</sup>Z. K. Tang, G. K. L. Wong, P. Yu, M. Kawasaki, A. Ohtomo, H. Koinuma, and Y. Segawa, *Appl. Phys. Lett.* **72**, 3270 (1998).
- <sup>6</sup>E. F. Schubert and J. K. Kim, *Science* **308**, 1274 (2005).
- <sup>7</sup>N. E. Hsu, W. K. Hung, and Y. F. Chen, *J. Appl. Phys.* **96**, 4671 (2004).
- <sup>8</sup>K. Vanheusden, W. L. Warren, C. H. Seager, D. R. Tallant, J. A. Voigt, and B. E. Gnade, *J. Appl. Phys.* **79**, 7983 (1996).
- <sup>9</sup>M. K. Kennedy, F. E. Kruis, H. Fissan, B. R. Mehta, S. Stappert, and G. Dumpich, *J. Appl. Phys.* **93**, 551 (2003).
- <sup>10</sup>M. K. Kennedy, F. E. Kruis, H. Fissan, H. Nienhaus, A. Lorke, and T. H. Metzger, *Sens. Actuators B* **108**, 62 (2005).
- <sup>11</sup>P. Ifeacho, H. Wiggers, and P. Roth, *Proc. Combust. Inst.* **30**, 2577 (2005); P. Ifeacho, T. Hülser, H. Wiggers, C. Schulz, and P. Roth, *Proc. Combust. Inst.* (in press).
- <sup>12</sup>K.-H. Hellwege and O. Madelung, *Landolt-Börnstein: Zahlenwerte und Funktionen aus Naturwissenschaft und Technik III* (Springer-Verlag, Berlin, 1982), Bd. 17f.
- <sup>13</sup>J. Zhang and L. Gao, *J. Solid State Chem.* **177**, 1425 (2005).
- <sup>14</sup>R. S. Katiyar, P. Dawson, M. M. Hargreave, and G. R. Wilkinson, *J. Phys. C* **4**, 2421 (1971).
- <sup>15</sup>K. N. Yu, Y. Xiong, Y. Liu, and C. Xiong, *Phys. Rev. B* **55**, 2666 (1997).
- <sup>16</sup>J. Zuo, C. Xu, X. Liu, C. Wang, Y. Hu, and Y. Qian, *J. Appl. Phys.* **75**, 1835 (1994).
- <sup>17</sup>Z. W. Chen, J. K. L. Lai, and C. H. Shek, *Phys. Rev. B* **70**, 165314 (2004).
- <sup>18</sup>J. F. Scott, *J. Chem. Phys.* **53**, 852 (1970).
- <sup>19</sup>F. Matossi, *J. Chem. Phys.* **19**, 1543 (1951).
- <sup>20</sup>H. Richter, Z. P. Wang, and L. Ley, *Solid State Commun.* **39**, 625 (1981).
- <sup>21</sup>I. H. Campbell and P. M. Fauchet, *Solid State Commun.* **58**, 739 (1986).